Robust Phased Array Navigation in Reflective Prone Areas

Oliver Hasler
Department of Engineering Cybernetics - NTNU
Trondheim, Norway
oliver.hasler@ntnu.no

Torleiv H. Bryne
Department of Engineering Cybernetics - NTNU
Trondheim, Norway
torleiv.h.bryne@ieee.org

Tor Arne Johansen
Department of Engineering Cybernetics - NTNU
Trondheim, Norway
tor.arne.johansen@ntnu.no

***Abstract*—Airborne robotic exploration require robust and reliable navigation solutions. If a mission is conducted in an environment where GNSS based navigation is potentially unreliable or completely unavailable, other navigation solutions must be established. The position estimation of the vehicle with a Phased Array Radio System (PARS) is one such possibility. The PARS used in these experiments is mainly thought to be used as a communications device between the vehicle and a ground station. As a secondary function, it is used to aid the inertial navigation system (INS) of the Unmanned Aerial Vehicle (UAV). Such a system can either be an additional level of security, act as a failsafe in case the primary navigation sensor is unavailable (GNSS dropout), or as an augmentation to an INS (additional sensor input) to increase navigation robustness and accuracy.**

A PARS navigation solution such as described in this paper has been developed and tested before. These tests have shown that a potential issue for the INS are the reflections of the communications beam on the water or ice surface. This does not affect the communication quality but has a big impact on the INS and therefore on the navigation quality and robustness. These reflections pose an even bigger problem, if the UAV is flown over the ocean or a flat snow- and ice-covered area, such as the arctic ice sheet.

The aim of this work is to investigate ways to increase the robustness of such a navigation system and to increase its reliability in an environment which is prone to radio wave reflections. The main focus lies in the adaptation of the position estimation algorithm to be more robust against horizontal reflections and to use error additional models to detect and handle these reflections in the navigation solution. The method presented in this paper is tested on experimental data, using a Radionor CRE2-189 as a ground antenna and a Radionor CRE2-144-LW antenna in an airborne vehicle.

The INS gets sensor inputs from a tactical-grade Inertial Measurement Unit (IMU), a GNSS receiver from ublox and a barometer from the Pixhawk flight controller, as well as the PARS mentioned above.

A navigation solution using the PARS (GNSS denied navigation) is compared to the navigation solution based on GNSS (see fig. 11). Improving the robustness and reliability of a lightweight GNSS free navigation solution allows for a multitude of new missions in GNSS detested areas, or areas where GNSS aided INS could become unreliable.

TABLE OF CONTENTS

978-1-6654-3760-8/22/$31.00 ©2022 IEEE

1. INTRODUCTION

Global Navigation Satellite System (GNSS) receivers are the primary navigation solution for unmanned aerial vehicles (UAVs). Such systems offer many obvious advantages, such as low cost, global coverage, lightweight receivers and high accuracy. However, with these advantages come several downsides. The low Signal-To-Noise (SNR) ratio of GNSS navigation systems makes these systems prone to jamming and spoofing [1]. Furthermore, GNSS coverage might be affected by high activity in the electromagnetic spectrum, by space weather phenomena's such as solar storms, or navigating close to the magnetic north or south pole.

In order to demote this problem, a redundant navigation solution has to be developed. When used in conjunction with an existing navigation solution, this helps to mitigate navigation loss through single point of failure. It furthermore lowers the dependence on third party infrastructure and hardware.

The system presented in this paper is an Inertial Navigation System (INS), aided by a Phased Array Radio System (PARS). The institute for technical cybernetics at the NTNU has several years of experience with research into PARS aided navigation systems [2] [1]. It has been an aim of the institute for technical cybernetics to develop a drift free, GNSS independent navigation solution which can be used to navigate safely in a GNSS deprived or GNSS denied environment.

Main contribution

The elevation, azimuth and range measurements provided by the PARS communications system are used to estimate the UAV position, not unlike the way they would be used in a conventional radar system. In case the communications link is reflected on a ground surface, the elevation, range and/or azimuth are corrupted. If this measurement is not rejected, this leads to an erroneous measurement update, which increases the estimation error of the INS. In case there are many such reflections within a given timeframe, the

position estimation of the UAV will be corrupted to a degree, where the Kalman filter may start to diverge. The method presented here tries to prevent this.

In case the range ρ and the unit bearing vector $\mathbf{b}$ are treated separately, reflections can be detected more easily. Furthermore, the separation of the range and the bearing measurement makes it possible to progress and these two measurements separately in future improvements.

Such an approach will furthermore allow for an algorithm which doesn't treat the complete measurement vector as an outlier in case a reflection has happened, but only the measurement which has been altered beyond a threshold by the reflection.

This algorithm is implemented in a ECEF framework (see 2). Tracking in this clearly defined coordinate frame has several advantages over tracking in a local coordinate frame. The most important advantages are:

- Multiple PARS (or other sensors) can be used to track a UAV over a large geographical area (navigation with data from multiple sensors).
- Easier integration of the UAV into a controlled airspace, since the ECEF WGS-84 coordinate frame is a well-defined datum.

Paper overview

After the Introduction above, this paper outlines some preliminaries in section 2. Section 3, goes through the equipment and setup used for the data generation for these experiments. In section 4 the algorithm for the position estimation in with the PARS is explained. Section 5 explains the algorithm for the navigation solution. Results from applying this approach on the flight test data is presented in section 6. Section 7 and section 8 contains a summary and an outlook to future work and potential ideas for future improvements.

2. PRELIMINARIES

Notation

The Euclidean vector norm is denoted $\|\cdot\|$. The $n \times n$ identity matrix is denoted $\mathbf{I_n}$. Moreover, a transpose of a vector or matrix $\mathbf{M}$ is denoted $\mathbf{M}^\top$.

Coordinate frames are denoted with $\{\cdot\}$. $\mathbf{S}(\cdot) \in SO(3)$ represents a skew symmetric matrix (e.g. $\mathbf{S(z_1)z_2} = \mathbf{z_1} \times \mathbf{z_2}$ where $\mathbf{z_1}, \mathbf{z_2} \in \mathbb{R}^3$. Additionally, $\mathbf{z^a_{bc}} \in \mathbb{R}^3$ denotes a vector $\mathbf{z}$, from frame $\{b\}$ to frame $\{c\}$ decomposed in frame $\{a\}$.

$\otimes$ denotes the Hamiltonian quaternion product, and $\odot$ is the Hadamard product.

$\mathbf{R^b_a} \in SO(3)$ is a rotation matrix, describing the rotation from frame $\{a\}$ to frame $\{b\}$. Such a rotation may also be represented by the quaternion $\mathbf{q^b_a} = (s, \mathbf{v}^\top)^\top$ where $s \in \mathbf{R}^1$ is the real part of a quaternion and $\mathbf{v} \in \mathbb{R}^3$ is the vector part.

Latitude and longitude on earth are represented by $\mu \in [-\pi/2, \pi/2]$ and $\lambda \in (-\pi, \pi]$.

Coordinate Systems

Four different coordinate systems were used in this paper (see fig. 1). The Earth Centered Inertial (ECI) frame, denoted $\{i\}$. The Earth Centered Earth Fixed (ECEF) frame, denoted $\{e\}$. And the Body frame of the UAV, denoted $\{b\}$. Furthermore, the reference frame of the PARS antenna is denoted $\{r\}$. The antenna frame $\{\mathrm{r}\}$ is simply a rotation of a local NED coordinate frame $\{\mathrm{n}\}$ around its down-axis [3].

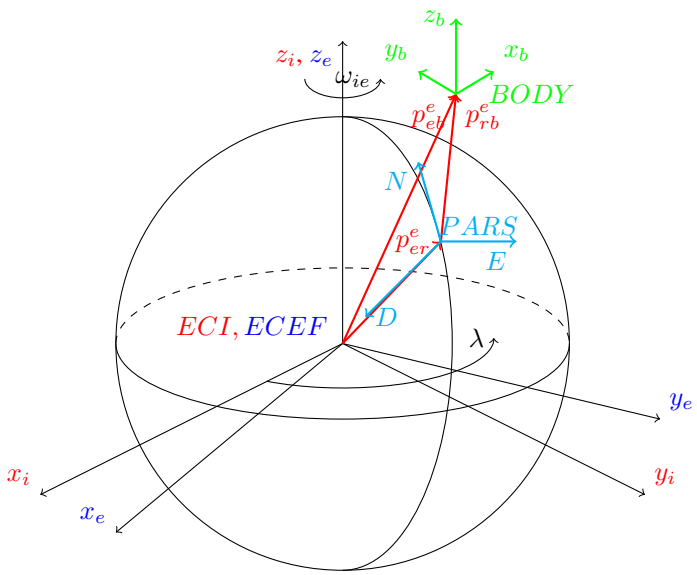

Figure 1. Definition of the BODY, ECEF, ECI and PARS frame

Attitude representations and relationships

In this paper, quaternions using the Hamiltonian representation are used to describe the UAV attitude. The unit quaternion for a rotation from frame $\{\gamma\}$ to frame $\{\beta\}$ looks as follows:

$$\mathbf{q}^\gamma_\beta = \begin{pmatrix} q_s \\ \mathbf{q}_v \end{pmatrix} = \begin{pmatrix} q_s \\ q_x \\ q_y \\ q_z \end{pmatrix} \in \mathbb{H} \tag{1}$$

$\mathbb{H}$ is defined as follows: [4]

$$\mathbb{H} := \mathbf{q}^\gamma_\beta \otimes \mathbf{q}^{\gamma\star}_\beta = 1 \;\; ; \;\; q_s \in \mathbb{R}^1 \;\; ; \;\; \mathbf{q}_v \in \mathbb{R}^3 \tag{2}$$

The quaternion can be used to calculate the rotation matrix $\mathbf{R}^\gamma_\beta \in SO(3)$ [4]

$$\mathbf{R}^\gamma_\beta = f(\mathbf{q}^\gamma_\beta) = \left(q_s - \mathbf{q}_v^\top \mathbf{q}_v\right) \mathbf{I}_3 + 2\mathbf{q}_v\mathbf{q}_v^\top + 2q_s\mathbf{S}(\mathbf{q}_v) \tag{3}$$

The Hamilton quaternion product ($\otimes$), is given as follows: [4]

$$\mathbf{q}_3 = \mathbf{q}_1 \otimes \mathbf{q}_2 = \begin{pmatrix} q_{s\,1}q_{s\,2} - \mathbf{q}_{v\,1}^\top \mathbf{q}_{v\,2} \\ q_{s\,1}\mathbf{q}_{v\,2} + q_{s\,2}\mathbf{q}_{v\,1} + \mathbf{q}_{v\,1} \times \mathbf{q}_{v\,2} \end{pmatrix} \tag{4}$$

The kinematic equation of a given unit quaternion is given as

follows: [1] [4] [3]

$$\dot{\mathbf{q}} = \frac{1}{2}\mathbf{q} \otimes \omega = \frac{1}{2}\mathbf{\Omega}(\omega)\mathbf{q} \tag{5}$$

$$\mathbf{\Omega}(\omega) = \begin{pmatrix} 0 & -\omega^\top \\ \omega & -S(\omega) \end{pmatrix}$$

The conjugate of a quaternion is given as follows:

$$\mathbf{q}^\star = \begin{pmatrix} q_s \\ -\mathbf{q}_v \end{pmatrix} \tag{6}$$

Additionally, the Euler angles are given as follows, with ϕ = roll, θ = pitch and ψ = yaw:

$$\mathbf{\Theta} = (\phi, \theta, \psi)^\top \tag{7}$$

The true attitude is denoted $\mathbf{q}$, while the attitude error quaternion is denoted $\delta\mathbf{q}$. The quaternion representing the attitude estimated by the INS algorithms is given as $\hat{\mathbf{q}}$ below.

$$\hat{\mathbf{q}} = \mathbf{q}_{INS} \otimes \delta\mathbf{q} \tag{8}$$

The three-dimensional attitude error parameterization of $\delta\mathbf{q}$ is the modified Rodrigues parameter: [5]

$$\delta\mathbf{q} = 4 \cdot \delta\mathbf{a}_{mrp} = 4 \cdot \frac{\delta\mathbf{q}_v}{1 + \delta q_s} \tag{9}$$

Inertial Measurement Unit

An IMU can be described in the following simplified measurement model. Specific forces and angular rate sensor (ARS) measurements are given as follows: [3]

$$\mathbf{f}^b_{IMU} = \mathbf{f}^b_{ib} + \mathbf{b}^b_{acc} + \boldsymbol{\varepsilon}^b_{acc} \tag{10}$$

$$\boldsymbol{\omega}^b_{IMU} = \boldsymbol{\omega}^b_{ib} + \mathbf{b}^b_{ars} + \boldsymbol{\varepsilon}^b_{ars} \tag{11}$$

Where $\mathbf{f}^b_{ib}$ represents the specific force, relating to the acceleration, and $\mathbf{g}^e_b$ represents the gravity vector (see eq. (12)). The variable $\boldsymbol{\omega}^b_{ib}$ represents angular velocity, while $\mathbf{v}^b_{ib}$ and $\mathbf{a}^b_{ib}$ represents the linear velocity, resp. acceleration in the BODY frame [6] [3].

$$\begin{aligned} \mathbf{f}^b_{ib} &= \mathbf{R}^b_e \cdot \dot{\mathbf{v}}^e_{ib} - \mathbf{R}^b_e \cdot \mathbf{g}^e_b \\ &= \mathbf{a}^b_{ib} + \mathbf{S}\left(\boldsymbol{\omega}^b_{ib}\right) \cdot \mathbf{v}^b_{ib} - \mathbf{R}^b_e \cdot \mathbf{g}^e_b \end{aligned} \tag{12}$$

$$\mathbf{g}^e_b = \boldsymbol{\gamma}^e_{ib} + \boldsymbol{\omega}_{ie} \begin{pmatrix} 1 & 0 & 0 \\ 0 & 1 & 0 \\ 0 & 0 & 0 \end{pmatrix} \mathbf{r}^e_{eb} \tag{13}$$

$\mathbf{S}\left(\boldsymbol{\omega}^b_{ib}\right) \cdot \mathbf{v}^b_{ib}$ describes the centripetal accelerations. $\boldsymbol{\gamma}^e_{ib}$ describes the gravitational acceleration [6]. The accelerometer (acc) biases are described in $\mathbf{b}^b_\star$. Whereas, the angular-rate-sensor (ars) biases are described by: $\boldsymbol{\omega}^b_\star$.

Kinematics - Strapdown Equations

The position and velocity of the BODY frame relative to the ECEF frame is represented by $\mathbf{p}^\mathbf{e}_\mathbf{eb} \in \mathbb{R}^{\not\Vdash}$ and $\mathbf{v}^\mathbf{e}_\mathbf{eb} \in \mathbb{R}^{\not\Vdash}$. These vectors are decomposed in the ECEF frame, as the superscript {e} indicates. The attitude between the BODY and the ECEF frame is given as the unit quaternion $\mathbf{q}^\mathbf{e}_\mathbf{b}$, while the angular velocity of the BODY frame relative to the ECEF frame is given as $\boldsymbol{\omega}^e_{eb} \in \mathbb{R}^{\not\Vdash}$. The strapdown equations following the explanations mentioned above are:

$$\dot{\mathbf{p}}^e_{eb} = \mathbf{v}^e_{eb} \tag{14}$$

$$\dot{\mathbf{v}}^e_{eb} = -2 \cdot \mathbf{S}\left(\boldsymbol{\omega}^e_{ie}\right) \mathbf{v}^e_{eb} + \mathbf{R}^e_b\left(\mathbf{q}^e_b\right) \cdot \mathbf{f}^b_{eb} + \mathbf{g}^e_b \tag{15}$$

$$\dot{\mathbf{q}}^e_b = \frac{1}{2} \cdot \mathbf{\Omega}\left(\boldsymbol{\omega}^b_{eb}\right) \cdot \mathbf{q}^e_b \tag{16}$$

$\mathbf{f}^b_{eb}$ represents the specific force acting on the UAV.

$$\mathbf{f}^b_{eb} = \left(\mathbf{R}^e_b\right)^\top \left(\mathbf{q}^e_b\right) \dot{\mathbf{v}}^e_{eb} \cdot + \left(\mathbf{R}^e_b\right)^\top \left(\mathbf{q}^e_b\right) \mathbf{g}^e_b \tag{17}$$

3. SENSORS AND EQUIPMENT

Phased Array Radio System

The communication between the ground station and the UAV was established with a PARS stationary on the ground (Radionor CRE-189), and a radio transceiver on the UAV (Radionor CRE2-144-LW). This communications setup is IP based and enables the operator to exchange a considerable amount of data with the UAV. Initialization of the communications link is established by an initial "ping" broadcasted by the ground-based PARS antenna. The direction of the reply from the airborne counterpart can be determined by the phase difference and time delay of the receiving signal on the different antenna arrays. Using this data, a PARS processing unit computes the elevation and azimuth of the communications beam. The range of the UAV can be determined by the round-trip time of a message. After the communication has been established, the PARS array communicates through a directional beam with the UAV. The azimuth and elevation needed to keep the communications beam pointed at the UAV are continuously updated by the PARS processing unit. The azimuth, elevation and range allow estimating the position of the UAV. This position estimate, sent to the UAV, can be used to correct the position estimation of the Inertial Navigation System (INS), allowing for a drift free navigation solution.

The communication rates of the Radionor CRE2 PARS are as follows: [1]

Distance	Rate
20 km	15 Mbit/s
30 km	7 Mbit/s
60 km	2.3 Mbit/s

Table 1. Communication rates of PARS antenna

IMU / GNSS / Barometer and data synchronization

A high-quality MEMS (Microelectromechanical systems) based IMU (Inertial Measurement Unit) from Sensonor, the Sensonor STIM300, was used for these experiments and the data generation. The IMU was configured to record angular

and lateral accelerations with a rate of 250 Hz. [7]. The INS position estimates are corrected by other aiding sensors (see Fig. 3). Apart from the PARS, the aiding sensors include a GNSS receiver and a barometer. An Ublox Neo-M8T GNSS receiver was used in this case. This sensor is used to incorporate satellite navigation data into the navigation solution, which can later be used as a reference. The GNSS receiver was configured to output raw GNSS observables. In combination with correction data from a ground station through RTKLIB, this allowed to derive high accuracy real-time kinematics (RTK) positioning. An Odroid XU4 running Dune was used as onboard computer. This onboard computer was connected to a Pixhawk 3 Pro autopilot, running ArduPilot flight control software. The autopilot contained an integrated magnetometer, barometer and a low grade IMU. A SenTiBoad was used to timestamp the IMU, GNSS and barometer measurements for later post flight analysis. [8]

4. POSITIONING BY PARS

As described in section 3, the PARS-based navigation system relies on the measurement of a number of physical quantities. These will be elucidated in the following section.

The tracking of the UAV was done in an ECEF coordinate frame. However, the PARS provides measurements in a local reference frame of the PARS system $\{\mathrm{r}\}$. The measurements provided by the PARS have therefore to be transformed into the ECEF coordinate frame. In order to be able to do this, the position and orientation of the PARS antenna in the ECEF frame must be known. These properties (latitude μ, longitude λ, height h and orientation of the PARS base antenna) were measured before the experiment and used to calculate the rotation matrix $\mathbf{R}_r^e \in \mathbb{R}^3$. In case the PARS antenna were positioned on a moving platform such as a ship or ground vehicle, the position of the PARS antenna would have to be measured and updated continuously.

The unit bearing vector $\hat{\boldsymbol{\eta}}_{rb}^r$ is calculated in the local PARS-antenna framework as follows:

$$\rho_{rb}^r = \rho_{rb\_m}^r + \varepsilon_\rho \tag{18}$$
$$\psi^r = \psi_m^r + \varepsilon_\psi \tag{19}$$
$$\alpha^r = \alpha_m^r + \varepsilon_\alpha \tag{20}$$

ρ_{rb}^r represents the range from the PARS antenna to the BODY frame. ψ^r is the azimuth measured in the PARS antenna frame and α^r is the elevation measured in the PARS antenna frame (see fig. 2). The subscript $\{\mathrm{m}\}$ indicates, that it is a measured value. The subscript $\{\mathrm{rb}\}$ indicates that this is a measurement from the PARS frame $\{\mathrm{r}\}$ to the BODY frame $\{\mathrm{b}\}$ which in this case is the position of the UAV.

The value $\varepsilon_\star$ represent the difference between the measured and the true value of the respective variable. If not stated otherwise, it is assumed that the errors are normally distributed with zero mean:

$$\varepsilon_\star \sim \mathcal{N}(0,\, \sigma^2) \tag{21}$$

The unit vector $\hat{\mathbf{p}}_{rb}^r$ represents the bearing vector pointing from the PARS frame $\{r\}$ to the BODY frame $\{b\}$ decomposed in the radio frame $\{r\}$ (See fig. 2). It is calculated as follows:

$$\begin{aligned} \boldsymbol{\eta}_{rb}^r &= \begin{pmatrix} x_{rb}^r \\ y_{rb}^r \\ z_{rb}^r \end{pmatrix} = \begin{pmatrix} \cos(\psi^r)\cdot\cos(\alpha^r) \\ \sin(\psi^r)\cdot\cos(\alpha^r) \\ -\sin(\alpha^r) \end{pmatrix} \; ; \|\boldsymbol{\eta}_{rb}^r\| = 1 \\ \hat{\mathbf{p}}_{rb}^r &= \rho_{rb}^r \cdot \boldsymbol{\eta}_{rb}^r \end{aligned} \tag{22}$$

The vector $\mathbf{p}_{er}^e$ can be derived from the longitude μ, latitude λ and height h measurements prior to experiment. The UAV position can be determined in the ECEF framework as follows:

$$\mathbf{p}_{eb}^e = \mathbf{p}_{er}^e + \mathbf{R}_r^e \cdot (\hat{\mathbf{p}}_{rb}^r \odot \mathbf{V}_{rae}) \cdot \rho_{rb}^r \tag{23}$$

The vector $\mathbf{V}_{rae}$ contains the values to correct measurements: [9]

$$\mathbf{V}_{rae} = \begin{pmatrix} b_\psi^{-1} b_\alpha^{-1} \\ b_\psi^{-1} b_\alpha^{-1} \\ b_\alpha^{-1} \end{pmatrix}$$

$$b_\psi = \mathbb{E}\left[\cos(\varepsilon_\psi)\right] = e^{-\frac{1}{2}\sigma_\psi^2}$$

$$b_\alpha = \mathbb{E}\left[\cos(\varepsilon_\alpha)\right] = e^{-\frac{1}{2}\sigma_\alpha^2}$$

and:

$$\mathbf{R}_r^e = f(\boldsymbol{\Theta}_{PARS})$$

$$\mathbf{p}_{er}^e = f(\boldsymbol{\Theta}_{PARS})$$

The σ_ψ and σ_α are provided by the supplier of the PARS system. The values used for the calculations in this paper are listed in table 2 [1].

σ_ψ	$(\pm 2^\circ)^2$
σ_α	$(\pm 2^\circ)^2$
σ_r	$(15\,\mathrm{m})^2$

Table 2. Variance of the range and angle measurements of the CRE-189 antenna

The vector $\boldsymbol{\Theta}_{PARS}$ represents the position of the PARS antenna in the ECEF frame of reference. In this case, this vector is determined before the experiment and stays constant. In case the ground PARS is mounted on a moving platform, this vector has to be updated dynamically.

Calibration of PARS base station position

In order to determine the vector $\boldsymbol{\Theta}_{\mathbf{PARS}}$ and through that $\mathbf{p}_{\mathbf{er}}^{\mathbf{e}}$ and $\mathbf{R}_{\mathbf{r}}^{\mathbf{e}}$, the PARS position on the ground has been measured with GNSS. The orientation of the antenna was determined with a compass.

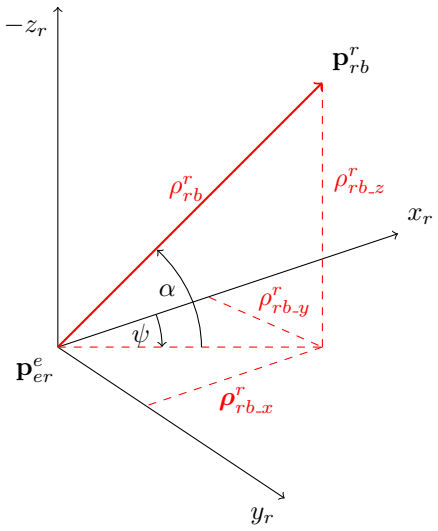

Figure 2. Illustration of the UAV in the PARS frame

5. Navigation System

The UAV state vector is described as follows:

$$\hat{\mathbf{x}}_{ins} = \left(\mathbf{p}^e_{eb\_ins}, \mathbf{v}^e_{eb\_ins}, \mathbf{q}^e_{eb\_ins}, \mathbf{b}^b_{acc\_ins}, \mathbf{b}^b_{ars\_ins}\right) \quad (24)$$

We obtain the following kinematic model, by applying the kinematics mentioned in section 2 (see also fig. 3).

$$\sum\nolimits_1 : \begin{cases} \dot{\hat{\mathbf{a}}}^e_{eb} & = -2 \cdot \mathbf{S}\left(\boldsymbol{\omega}^e_{ie}\right) \cdot \hat{\mathbf{v}}^e_{eb} + \mathbf{R}^e_{b\ avg}(\mathbf{q}^e_b) \cdot \hat{\mathbf{f}}^b_{ib} + \mathbf{g}^e_b\left(\mathbf{p}^e_{eb}\right) \\ \dot{\hat{\mathbf{v}}}^e_{eb} & \leftarrow \hat{\mathbf{v}}^e_{eb} + \hat{\mathbf{a}}^e_{eb} \cdot T_s \\ \dot{\hat{\mathbf{p}}}^e_{eb} & \leftarrow \hat{\mathbf{p}}^e_{eb} + \hat{\mathbf{v}}^e_{eb} \cdot T_s + \frac{1}{2} \cdot T_s^2 \cdot \hat{\mathbf{a}}^e_{eb} \\ \hat{\boldsymbol{\omega}}^b_{eb} & = \boldsymbol{\omega}^b_{IMU} - \hat{\mathbf{b}}^b_{ars\ tot} - \mathbf{R}^b_e \boldsymbol{\omega}^e_{ie} \\ \dot{\hat{\mathbf{q}}}^e_b & \leftarrow \frac{1}{2}\hat{\mathbf{q}}^e_b \otimes \delta\mathbf{q}\left(\hat{\boldsymbol{\omega}}^b_{eb}, T_s\right) \end{cases} \quad (25)$$

For every new IMU measurement, the covariance matrix is updated as follows:

$$\sum\nolimits_2 : \begin{cases} \boldsymbol{\Phi} & \leftarrow \mathbf{I}_{15x15} + \mathbf{F} \cdot T_s \\ \tilde{\mathbf{P}} & \leftarrow \boldsymbol{\Phi}\hat{\mathbf{P}}\boldsymbol{\Phi}^\top + \mathbf{Q}_d \\ \hat{\mathbf{P}} & \leftarrow \frac{1}{2} \cdot \left(\tilde{\mathbf{P}} + \tilde{\mathbf{P}}^\top\right) \end{cases} \quad (26)$$

The matrixes $\mathbf{F}$ and $\mathbf{Q}_d$ are given in Appendix 8

Multiplicative Extended Kalman Filter (MEKF)

The error state vector $\delta\hat{\mathbf{x}}$ is described as follows:

$$\delta\hat{\mathbf{x}} = \left(\delta\hat{\mathbf{p}}, \delta\hat{\mathbf{v}}, \delta\hat{\mathbf{q}}, \delta\hat{\mathbf{b}}_{acc}, \delta\hat{\mathbf{b}}_{ars}\right) \quad (27)$$

The error-state vector is calculated for each aiding measurement (see fig. 3).

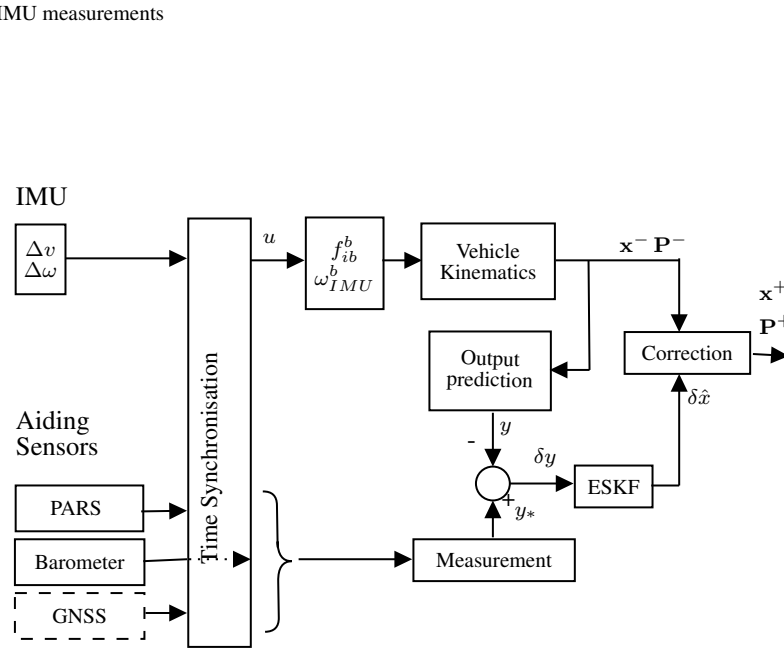

Figure 3. Shematic of architecture of the Navigation Solution

$\delta\hat{\mathbf{a}}$ represents the 3D attitude error and is used to calculate the attitude error quaternion $\delta\hat{\mathbf{q}}\left(\delta\hat{\mathbf{a}}\right)$.

The attitude error quaternion $\delta\hat{\mathbf{q}}\left(\delta\hat{\mathbf{a}}\right)$ is determined from the attitude change $\delta\hat{\mathbf{a}}$ as follows: [5]

$$\delta\tilde{\mathbf{q}}(\delta\hat{\mathbf{a}}) = \frac{1}{16 + (\delta\hat{\mathbf{a}})^\top(\delta\hat{\mathbf{a}})} \begin{pmatrix} 16 - (\delta\hat{\mathbf{a}})^\top(\delta\hat{\mathbf{a}}) \\ 8 \cdot \delta\hat{\mathbf{a}} \end{pmatrix} \quad (28)$$

Update of the state vector $\hat{\mathbf{x}}$ with error states in $\delta\hat{\mathbf{x}}$ is described in (29).

$$\sum\nolimits_3 : \begin{cases} \hat{\mathbf{p}} & \leftarrow \hat{\mathbf{p}} + \delta\hat{\mathbf{p}} \\ \hat{\mathbf{v}} & \leftarrow \hat{\mathbf{v}} + \delta\hat{\mathbf{v}} \\ \hat{\mathbf{q}} & \leftarrow \hat{\mathbf{q}} \otimes \delta\hat{\mathbf{q}} \\ \hat{\mathbf{b}}_{acc} & \leftarrow \hat{\mathbf{b}}_{acc} + \delta\hat{\mathbf{b}}_{acc} \\ \hat{\mathbf{b}}_{ars} & \leftarrow \hat{\mathbf{b}}_{ars} + \delta\hat{\mathbf{b}}_{ars} \end{cases} \quad (29)$$

The Kalman filter update with a new aiding measurement is done as follows:

$$\sum\nolimits_4 : \begin{cases} \mathbf{K} & \leftarrow \mathbf{P}\mathbf{H}^\top\left(\mathbf{H}\mathbf{P}\mathbf{H}^\top + \mathbf{R}\right)^{-1} \\ \tilde{\mathbf{P}} & \leftarrow \left(\mathbf{I} - \mathbf{K}\mathbf{H}\right)\hat{\mathbf{P}}\left(\mathbf{I} - \mathbf{K}\mathbf{H}\right)^\top + \mathbf{K}\mathbf{R}\mathbf{K}^\top \\ \hat{\mathbf{P}} & \leftarrow \frac{1}{2}\left(\tilde{\mathbf{P}} + \tilde{\mathbf{P}}^\top\right) \end{cases} \quad (30)$$

After the INS states have been corrected, the error state vector $\delta\hat{\mathbf{x}}$ is reset to 0.

PARS measurement equations

The linear position is calculated using equation [23]. So that the linear measurement matrix:

$$\mathbf{C} = (\mathbf{I}_3\ \mathbf{0}_{3x3}\ \mathbf{0}_{3x3}\ \mathbf{0}_{3x3}\ \mathbf{0}_{3x3}) \tag{31}$$

can be applied in the error state Kalman filter. Since the measurements are conducted in spherical coordinates and the tracking of the UAV with the error-state Kalman filter is conducted in Cartesian coordinates, the covariance must be mapped from spherical to Cartesian coordinates. Two different approaches were implemented to achieve this.

Linearization

In the "Linearized approach", the measurement vector $\mathbf{y}^r_{Rb}$ ($\mathbf{y}_\star$ in fig. 3) is linearized to the error vector $\boldsymbol{\epsilon}$.

$$\mathbf{M} = \frac{\partial \mathbf{y}^r_{Rb}}{\partial \boldsymbol{\epsilon}} = \begin{pmatrix} m_{11} & m_{12} & m_{13} \\ m_{21} & m_{22} & m_{23} \\ m_{31} & m_{32} & m_{33} \end{pmatrix} \tag{32}$$

The linearization can be calculated with $\boldsymbol{\epsilon}$ as given below and with $\mathbf{y}^r_{Rb}$ as stated in eq. (33):

$$\boldsymbol{\varepsilon} = (\varepsilon_\rho\ ; \varepsilon_\alpha\ ; \varepsilon_\psi)^\top$$

$\hat{\mathbf{y}}^r_{rb}$ is the position estimation from the PARS to the UAV which is de-biased with $\mathbf{V}_{rae}$ according to [9].

$$\hat{\mathbf{y}}^r_{rb} = \rho_{rb} \begin{pmatrix} x^r_{rb}(\alpha_m; \psi_m) \\ y^r_{rb}(\alpha_m; \psi_m) \\ z^r_{rb}(\psi_m) \end{pmatrix} = \rho_{rb} \boldsymbol{\eta}^r_{rb} \odot \mathbf{V}_{rae} \tag{33}$$

$\mathbf{V}_{rae}$ is given as follows:

$$\mathbf{V}_{rae} = (b_\alpha \cdot b_\psi, b_\alpha \cdot b_\psi, b_\psi)^\top \tag{34}$$

Determining the Jacobi matrix $\mathbf{M}$ yields the result, presented in (eq. (35)) - (eq. (43)). Substituting the trigonometric expressions with the correct corresponding terms results in the expressions in the right column.

$$m_{11} = \frac{\cos(\alpha)\cos(\psi)}{b_\alpha b_\psi} = x^r_{rb} \tag{35}$$

$$m_{12} = \frac{-\rho \cdot \sin(\alpha)\cos(\psi)}{b_\alpha b_\psi} = -\rho_{rb} y^r_{rb} \tag{36}$$

$$m_{13} = \frac{-\rho \cdot \cos(\alpha)\sin(\psi)}{b_\alpha b_\psi} = \frac{\rho_{rb} x^r_{rb} z^r_{rb} b_{\boldsymbol{\psi}}}{\sqrt{1 - (b_{\boldsymbol{\psi}} z^r_{rb})^2}} \tag{37}$$

$$m_{21} = \frac{\sin(\alpha)\cos(\psi)}{b_\alpha b_\psi} = y^r_{rb} \tag{38}$$

$$m_{22} = \frac{\rho \cdot \cos(\alpha)\cos(\psi)}{b_\alpha b_\psi} = \rho_{rb} x^r_{rb} \tag{39}$$

$$m_{23} = \frac{-\rho \cdot \sin(\alpha)\sin(\psi)}{b_\alpha b_\psi} = \frac{\rho_{rn} y^r_{rb} z^r_{rb} b_{\boldsymbol{\psi}}}{\sqrt{1 - (b_{\boldsymbol{\psi}} z^r_{rb})^2}} \tag{40}$$

$$m_{31} = \frac{\sin(\psi)}{b_\psi} = y^r_{rb} \tag{41}$$

$$m_{32} = 0 = 0 \tag{42}$$

$$m_{33} = \frac{-\rho \cdot \cos(\psi)}{b_\psi} = \frac{-\rho_{rb}\sqrt{1 - (b_{\boldsymbol{\psi}} z^r_{rb})^2}}{b_{\boldsymbol{\psi}}} \tag{43}$$

Eq. 44 shows how to calculate the linearized measurement covariance matrix $\mathbf{R}^e_{Rb}$, in the $\{e\}$ datum, with the covariance matrix represented in spherical coordinates $\mathbf{R}_{rbe}$ and the Jacobi matrix $\mathbf{M}$.

$$\mathbf{R}^e_{Rb} = \mathbf{R}^e_r \mathbf{M} \mathbf{R}_{\mathbf{rbe}} \mathbf{M}^\top \mathbf{R}^{e\top}_r \tag{44}$$

Approach according to Yakov Bar-Shalom

The second method which was implemented is based on the nonlinear coordinate transformation according to [9, Chapter 1.7]. The covariance matrix of the converted measurements, conditioned on the measurement values, is called: $\mathbf{R}_{YBS}$ in this paper.

Eq. 47 - eq. (52) represent the result of this substitution based on the equations provided in: [9, eq: 1.7.4-7 - 1.7.4-12].

$$\mathbf{R}_{\mathbf{YBS}} = \begin{pmatrix} R_{11} & R_{12} & R_{13} \\ R_{21} & R_{22} & R_{23} \\ R_{13} & R_{23} & R_{33} \end{pmatrix} \tag{45}$$

The trigonometric expressions in the covariance terms have been substituted by the corresponding terms dependent on the calculated values: $x^r_{Rb}; y^r_{Rb}; z^r_{Rb}$.

Eq. 46 shows the measurement covariance matrix $\mathbf{R}^e_{Rb}$ in $\{e\}$ coordinates based on the approach in of Yakov Bar Shalom [9].

$$\mathbf{R}^e_{Rb} = \mathbf{R}^e_r \mathbf{R}_{YBS} \mathbf{R}^{e\top}_r \tag{46}$$

$$R_{11} = \text{var}\left(\mathrm{x_m}|\mathrm{r_m}, \alpha_\mathrm{m}, \psi_\mathrm{m}\right)$$
$$= \left[1 - 2 \cdot \left(b_\alpha b_\psi\right)^2\right] \left(r_{Rb} \cdot x^r_{Rb}\right)^2 + \frac{1}{4}\left(r^2_{Rb} + \sigma^2_r\right) \left[1 + b^4_\alpha \cdot \left(1 - \frac{2\left(y^r_{Rb} b_\alpha b_\psi\right)^2}{1 - \left(z^r_{Rb} b_\psi\right)^2}\right)\right] \left[1 + b^4_\psi \left(1 - 2\left(z^r_{Rb} b_\psi\right)^2\right)\right] \tag{47}$$

$$R_{22} = \text{var}\left(\mathrm{y_m}|\mathrm{r_m}, \alpha_\mathrm{m}, \psi_\mathrm{m}\right)$$
$$= \left[1 - 2\left(b_\alpha b_\psi\right)^2\right] \left(r_{Rb} \cdot y^r_{Rb}\right)^2 + \frac{1}{4}\left(r^2_{Rb} + \sigma^2_r\right) \left[1 - b^4_\alpha \cdot \left(1 - \frac{2\left(y^r_{Rb} b_\alpha b_\psi\right)^2}{1 - \left(z^r_{Rb} b_\psi\right)^2}\right)\right] \left[1 + b^4_\psi \left(1 - 2\left(z^r_{Rb} b_\psi\right)^2\right)\right] \tag{48}$$

$$R_{33} = \text{var}\left(\mathrm{z_m}|\mathrm{r_m}, \alpha_\mathrm{m}, \psi_\mathrm{m}\right)$$
$$= \left(1 - 2b^2_\psi\right) \left(r_{Rb} \cdot z^r_{Rb}\right)^2 + \frac{1}{2}\left(r^2_{Rb} + \sigma^2_r\right) \left[1 - b^4_\psi \left(1 - 2\left(z^r_{Rb} b_\psi\right)^2\right)\right] \tag{49}$$

$$R_{12} = \text{cov}\left(\mathrm{x_m y_m}|\mathrm{r_m}, \alpha_\mathrm{m}, \psi_\mathrm{m}\right)$$
$$= \left[\left(b_1 b_2\right)^{-2} - 2\right] \cdot x^r_{Rb} \cdot y^r_{Rb} \cdot r_{Rb} + \frac{1}{2}\left(r^2_{Rb} + \sigma^2_r\right) b^4_\alpha \frac{x^r_{Rb} y^r_{Rb} \cdot \left(b_\alpha b_\psi\right)^2}{1 - \left(z^r_{Rb} b_\psi\right)^2} \left[1 + b^4_\psi \cdot \left(1 - 2 \cdot \left(z^r_{Rb} b_\psi\right)^2\right)\right] \tag{50}$$

$$R_{13} = \text{cov}\left(\mathrm{x_m}, \mathrm{z_m}|\mathrm{r_m}, \alpha_\mathrm{m}, \psi_\mathrm{m}\right)$$
$$= \left[\left(b_\alpha b_\psi\right)^2 + b^2_\psi - 1\right] \cdot x^r_{Rb} \cdot z^r_{Rb} \cdot r^2_{Rb} - \left(r^2_{Rb} + \sigma^2_r\right) b^2_\alpha b^6_\psi x^r_{Rb} z^r_{Rb} \tag{51}$$

$$R_{23} = \text{cov}\left(\mathrm{y_m}, \mathrm{z_m}|\mathrm{r_m}, \alpha_\mathrm{m}, \psi_\mathrm{m}\right)$$
$$= \left[\left(b_\alpha b_\psi\right)^2 + b^2_\psi - 1\right] \cdot y^r_{Rb} \cdot z^r_{Rb} \cdot r^2_{Rb} - \left(r^2_{Rb} + \sigma^2_r\right) b^2_\alpha b^6_\psi y^r_{Rb} z^r_{Rb} \tag{52}$$

6. RESULTS

In order to acquire the results presented in this section, the recorded flight test data has been run through the algorithm presented in this paper. Four different approaches are being compared in this section. (see: Tab. 6). Approach 1 and 2 in Tab. 6 use the bearing vector and range as introduced in section 4. These results are compared to approach 3 and 4 which are used as a reference.

	Method	Aiding Sensors
1:	Linearized covariance matrix conversion (see: section 5)	IMU / PARS
2:	Covariance matrix calculation acc. to YBS (see: section 5)	IMU / PARS
3:	Altitude measurement based on barometer	IMU / PARS Barometer
4:	Reference	GNSS

Table 3. algorithms compared

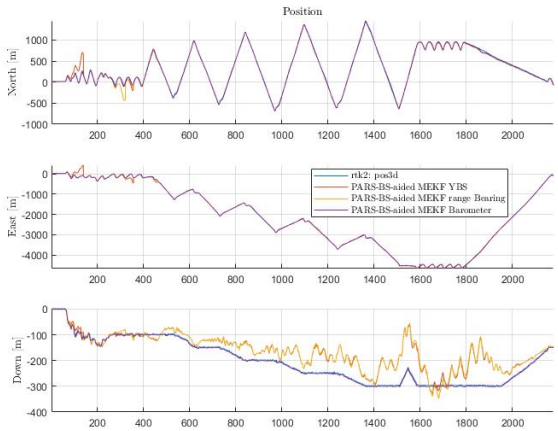

Figure 4. Position of the UAV in a NED coordinate frame (rotated $\{r\}$ frame)

Fig. 4 shows the position estimation in a local NED coordinate system with the PARS antenna positioned in the origin of the coordinate frame. The abscise of the plots represents flight time. The position estimation of the vehicle in "north" and "east" (horizontal to earths surface) fits closely to the reference position: "rtk2: pos3d" which is based on GNSS data. However, the altitude, for the first two cases mentioned in Tab. 6 (elevation (ε) measured by the PARS) is very inaccurate. The data for this investigation has been recorded on a flight over the ocean, which is a reflective surface for the PARS communications link. The reason for this poor quality in altitude estimation are mainly these reflections of the communication link on the water surface.

Furthermore, as can be seen in Fig. 6 and Fig. 7, the UAV was flying outside the 45° opening angle of the PARS antenna during the beginning and end of its flight. This 45° boundaries are marked with a red line in Fig. 6 and Fig. 7.

In Fig. 7 the boundaries are rotated by $\mathbf{R}^\mathbf{n}_\mathbf{r}$ to fit into the NED reference frame. The measured azimuth α^r and elevation ε^r shall be considered invalid in case the measured angles deviated more than 45° from the PARS normal axis. The behavior of the tracking algorithm when the UAV flies close to the PARS antenna shall therefore be ignored. This explains the erratic behavior of the tracking algorithm at the beginning and the end of the flight, as can be seen in Fig. 5 (area in proximity of the origin of the plot), and in Fig. 4 (beginning of the flight).

Fig. 8 displays the deviation of each method in an NED coordinate frame to method 4 in Tab. 6 (GNSS data).

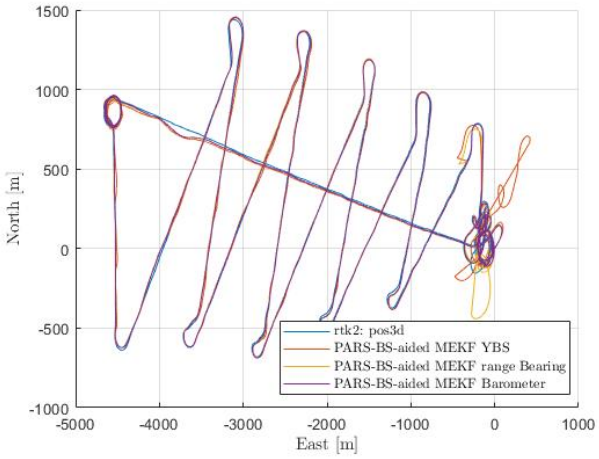

Figure 5. Horizontal flight path of the UAV in a NED coordinate frame (rotated $\{r\}$ frame)

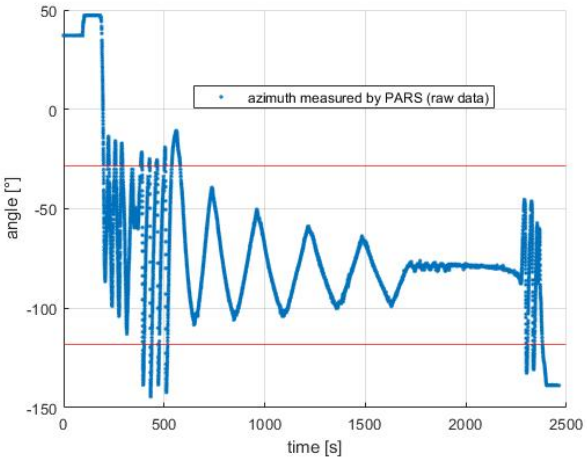

Figure 7. Azimuth measured by PARS

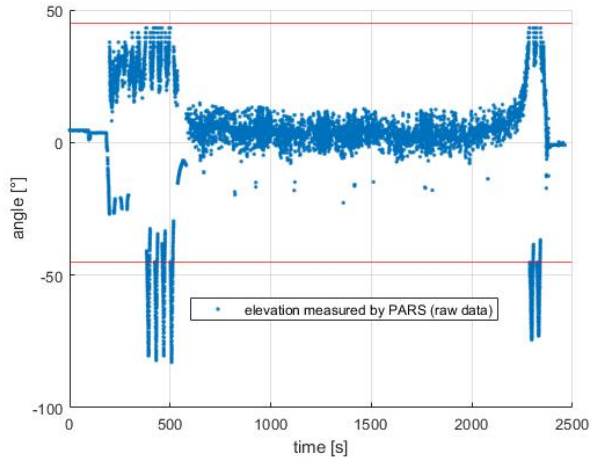

Figure 6. Elevation measured by PARS

The dotted lines in these figures represent the 3σ values. As can be seen, in Fig. 8, the accuracy of the PARS assisted INS navigation is very accurate in the "north" – "east" coordinate plane. However, in "down" direction of the NED-coordinate frame, the accuracy lies outside the dotted 3σ line. The reason for that are reflections of the PARS communications link on the earth surface. As mentioned already, the flights for this field trials were done over water, which is a very reflective surface for the PARS communications link. These reflections cause periodically big errors in the ESKF which cause the poor quality in altitude estimation (see also Fig. 12).

It is visible in Fig. 8, that the accuracy of approach 2 in Tab. 6 is slightly better in comparison to the approach with a linearized coordinate conversion (method 1 in Tab. 6). This is to be expected, since the linearization leads to a slightly "overconfident" algorithm. Besides, it is visible that in case an additional sensor is used for the position estimation (in this case a barometer) the position estimation becomes more accurate.

Furthermore, it is visible that the error in the "down" axis in Fig. 8 is very big in comparison to the method 3 from Tab. 6. As already mentioned, this is due to the reflections of the PARS communications beam on the water surface. A similar behavior can be seen when comparing the estimated velocities of the UAV (see Fig. 9) and the velocity error compared to the velocity measured with GNSS (see Fig. 10). In case a barometer was used to estimate the altitude, this erratic behavior cannot be seen.

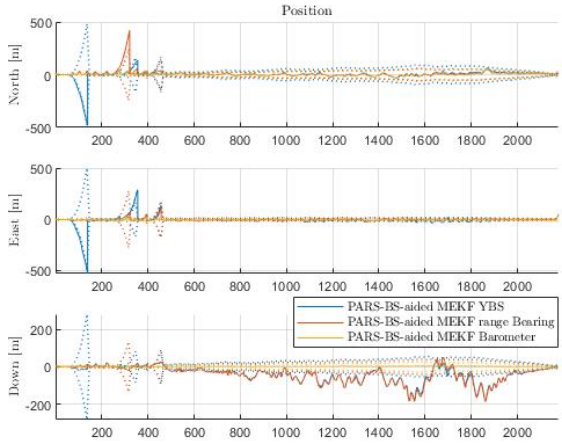

Figure 8. Position Error

7. Conclusions

The Figs. 11 and 12 show the measurement plots provided by the PARS in a horizontal plane (Fig. 11) and the altitude measurement plots (Fig. 12). The red plot in these figures is the GNSS reference. It is clearly visible, from these plots, that the water surface above which the UAV was flying poses a huge challenge for a navigation solution such as the one presented in this paper.

The algorithm to tracking in ECEF $\{e\}$ coordinates works as expected. This will furthermore allow tracking a target with multiple antennas in the same framework.

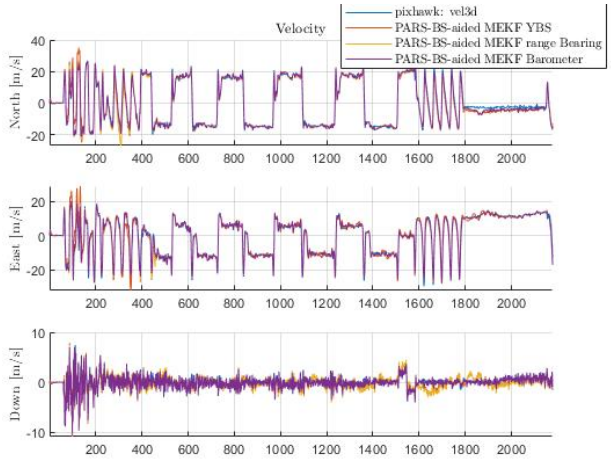

Figure 9. Comparison of velocity estimation with GNSS measured velocity

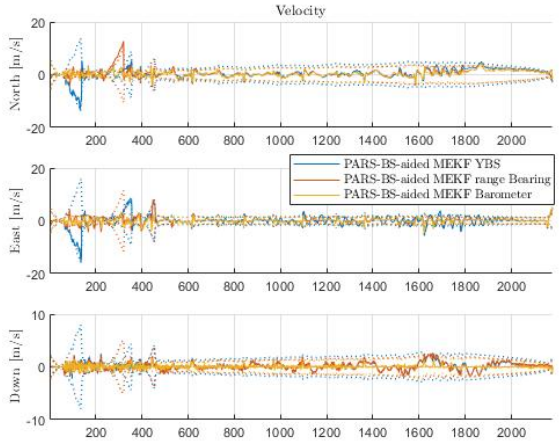

Figure 10. Comparison of velocity estimation relative to GNSS measured velocity

The introduced data structure will allow further development to correct the INS with range and bearing independently. (See. 8).

8. Future Work

As already mentioned in 7, the changes made to the algorithm will make it possible to change the navigation equations completely. Instead of propagating position, velocity and attitude, the range and the bearing vector will be propagated. This in retrospect will allow for better reflection detection and handling of the PARS communications beam.

Beside this change, there are other potential improvements which could be analyzed and developed. Among which is the usage of colored noise in the estimation algorithm. Currently, the covariance matrix in Cartesian coordinates is calculated as follows:

$$\mathbf{R}_{Rb} = \mathbf{M}\mathbf{R}_{rbe}\mathbf{M}^{\top} \tag{53}$$

With the covariance matrix in spherical coordinates (see also eq. (63)).

$$\mathbf{R}_{rbe} \neq f\left(r\right) \tag{54}$$

When analyzing fig. 12 and fig. 11 which show the plots in altitude vs time, resp. the plots in the north-east plane of the NED coordinate plane, the following occurs. In case there are many reflections on the water surface, the assumption that: $\epsilon_{\star} \sim \mathcal{N}(\prime, \sigma^{\in})$ may no longer hold. In this case, the covariance matrix for spherical coordinates could be altered as follows:

$$\mathbf{R}_{rbe}\left(\rho\right) = \begin{pmatrix} \sigma_r^2 & 0 & 0 \\ 0 & r^r\lambda_\alpha\sigma_\alpha^2 & 0 \\ 0 & 0 & r^r\lambda_\varepsilon\sigma_\varepsilon^2 \end{pmatrix} = f(r) \tag{55}$$

$\lambda_{\star}$ is a tuning factor, and r is the range. In case there are no reflections. It should be mentioned here, that this idea might need further evaluation.

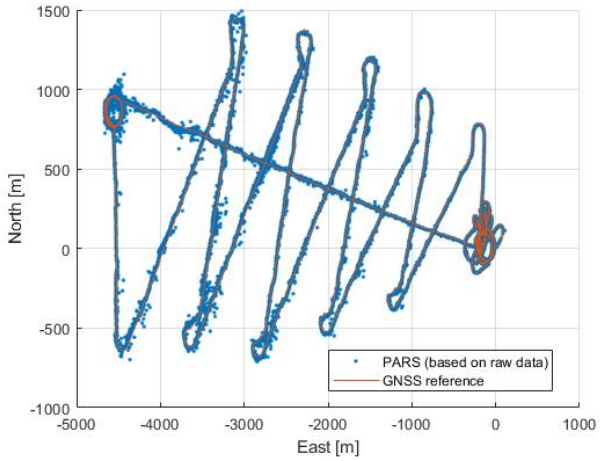

Figure 11. Horizontal plots calculated from raw PARS data

Appendix

MEKF matrixes

$$\mathbf{F}\left(t\right) = \begin{pmatrix} \mathbf{0}_{3x3} & \mathbf{I}_3 & \mathbf{0}_{3x3} & \mathbf{0}_{3x3} & \mathbf{0}_{3x3} \\ \mathbf{0}_{3x3} & -2\cdot\mathbf{S}\left(\boldsymbol{\omega}_{ie}^{e}\right) & \mathbf{V}_\alpha & \mathbf{V}_{acc} & \mathbf{0}_{3x3} \\ \mathbf{0}_{3x3} & \mathbf{0}_{3x3} & \mathbf{A}_\alpha & \mathbf{0}_{3x3} & \mathbf{A}_{ars} \\ \mathbf{0}_{3x3} & \mathbf{0}_{3x3} & \mathbf{0}_{3x3} & -\mathbf{T}_{acc}^{-1} & \mathbf{0}_{3x3} \\ \mathbf{0}_{3x3} & \mathbf{0}_{3x3} & \mathbf{0}_{3x3} & \mathbf{0}_{3x3} & -\mathbf{T}_{ars}^{-1} \end{pmatrix} \in \mathbb{R}^{15x15} \tag{56}$$

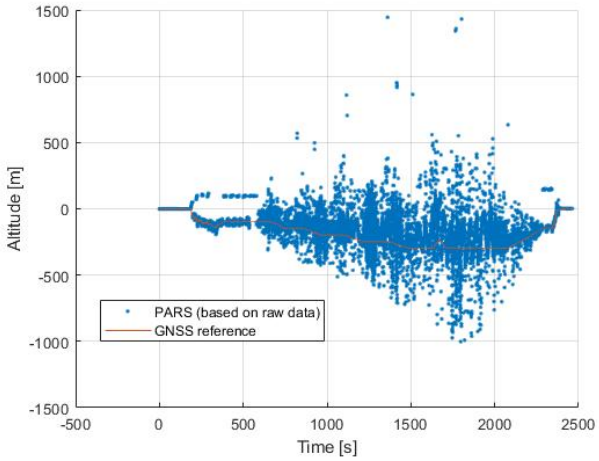

Figure 12. Altitude plots calculated from raw PARS data

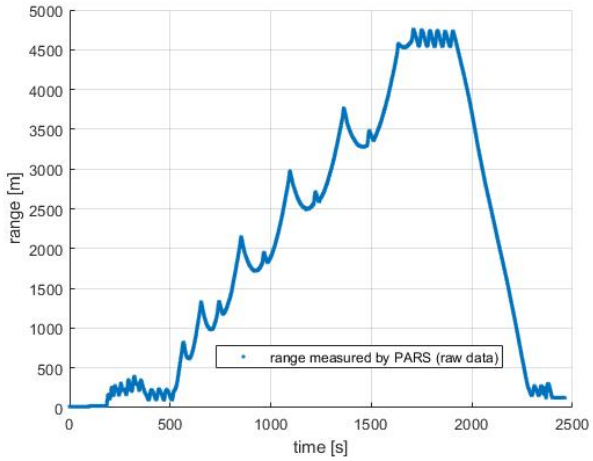

Figure 13. Altitude plots calculated from raw PARS data

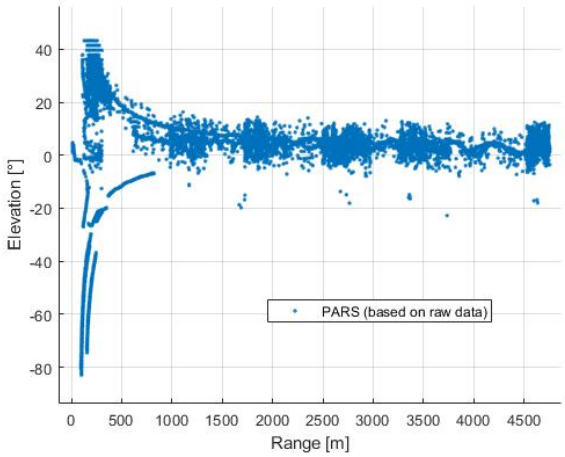

Figure 14. Altitude plots calculated from raw PARS data

$$\mathbf{G}(t) = \begin{pmatrix} \mathbf{0}_{3x3} & \mathbf{0}_{3x3} & \mathbf{0}_{3x3} & \mathbf{0}_{3x3} \\ -\mathbf{R}_b^e(\mathbf{q}_b^e) & \mathbf{0}_{3x3} & \mathbf{0}_{3x3} & \mathbf{0}_{3x3} \\ \mathbf{0}_{3x3} & -\mathbf{I}_3 & \mathbf{0}_{3x3} & \mathbf{0}_{3x3} \\ \mathbf{0}_{3x3} & \mathbf{0}_{3x3} & \mathbf{I}_3 & \mathbf{0}_{3x3} \\ \mathbf{0}_{3x3} & \mathbf{0}_{3x3} & \mathbf{0}_{3x3} & \mathbf{I}_3 \end{pmatrix} \in \mathbb{R}^{15x12} \tag{57}$$

$$\mathbf{V}_\alpha = -\hat{\mathbf{R}}_b^e(\hat{\mathbf{q}}_b^e)\,\mathbf{S}\left(\mathbf{f}_{ib\ imu}^b - \mathbf{b}_{acc\ ins}^b\right) \tag{58}$$

$$\mathbf{V}_{acc} = -\hat{\mathbf{R}}_b^e(\hat{\mathbf{q}}_b^e) \tag{59}$$

$$\mathbf{A}_\alpha = -\mathbf{S}\left(\boldsymbol{\omega}_{imu}^b - \mathbf{b}_{ars\ ins}^b\right) \tag{60}$$

$$\mathbf{A}_{ars} = -\mathbf{I}_3 \tag{61}$$

$$\mathbf{Q} = \begin{pmatrix} \mathbf{q}_{acc}^2 & 0 & 0 & 0 \\ 0 & \mathbf{q}_{ars}^2 & 0 & 0 \\ 0 & 0 & \mathbf{q}_{acc\ bias}^2 & 0 \\ 0 & 0 & 0 & \mathbf{q}_{ars\ bias}^2 \end{pmatrix} \tag{62}$$

$$\mathbf{R}_{rbe} = \begin{pmatrix} \mathbf{r}_{range}^2 & 0 & 0 \\ 0 & \mathbf{r}_{azi}^2 & 0 \\ 0 & 0 & \mathbf{r}_{elev}^2 \end{pmatrix} \tag{63}$$

$$\tilde{\mathbf{Q}} = \mathbf{GQG} \tag{64}$$

$$\begin{aligned} \mathbf{Q}_d \approx & \tilde{\mathbf{Q}} \cdot T_s + \frac{T_s^2}{2}\left(\mathbf{F}\tilde{\mathbf{Q}} + \tilde{\mathbf{Q}}\mathbf{F}^\top\right) \\ & + \frac{T_s^3}{6}\left(\mathbf{F}^2\tilde{\mathbf{Q}} + 2\mathbf{F}\tilde{\mathbf{Q}}\mathbf{F}^\top + \tilde{\mathbf{Q}}\left(\mathbf{F}^\top\right)^2\right) \\ & + \frac{T_s^4}{24}\left(\mathbf{F}^3\tilde{\mathbf{Q}} + 3\mathbf{F}^2\tilde{\mathbf{Q}}\mathbf{F}^\top + 3\mathbf{F}\tilde{\mathbf{Q}}\left(\mathbf{F}^\top\right)^2 + \tilde{\mathbf{Q}}\mathbf{F}^3\right) \end{aligned} \tag{65}$$

See. [3, Ch. 4]

ACKNOWLEDGMENTS

We thank the drone pilot Pål Kvaløy and the scientist Kristoffer Gryte for their commitment and hard work during these experiments.

REFERENCES

[1] G. Kristoffer, B. T. H., A. S. M., and J. T. A., "Field test results of gnss-denied inertial navigation aided by phased-array radio systems for uavs," in *2019 International Conference on Unmanned Aircraft Systems (ICUAS)*, 2019, pp. 1398–1406. DOI: 10.1109/ICUAS.2019.8798057.

[2] S. Albrektsen, T. Bryne, and T. Johansen, "Phased array radio system aided inertial navigation for unmanned aerial vehicles," Mar. 2018, pp. 1–11. DOI: 10.1109/AERO.2018.8396433.
[3] J. Farrell, *Aided Navigation: GPS with High Rate Sensors*, 1st ed. USA: McGraw-Hill, Inc., 2008, ISBN: 0071493298.
[4] J. Solà, "Quaternion kinematics for the error-state kalman filter," *arXiv preprint arXiv:1711.02508*, 2017. DOI: \url{https://doi.org/10.48550/arXiv.1711.02508}. arXiv: 1711.02508 [cs.RO].
[5] F. L. Markley, "Attitude error representations for kalman filtering," *Journal of Guidance, Control, and Dynamics*, vol. 26, no. 2, pp. 311–317, 2003. DOI: 10.2514/2.5048. eprint: \url{https://doi.org/10.2514/2.5048}. [Online]. Available: %5Curl%7Bhttps://doi.org/10.2514/2.5048%7D.
[6] P. Groves, *Principles of GNSS, Inertial, and Multisensor Integrated Navigation Systems, Second Edition*. Artech House, 2013.
[7] *Sensonor stim300 datasheet*, https://www.sensonor.com/products/inertial-measurement-units/stim300/.
[8] S. M. Albrektsen and T. A. Johansen, "User-configurable timing and navigation for uavs," eng, *Sensors (Basel, Switzerland)*, vol. 18, no. 30061522, p. 2468, Jul. 2018, ISSN: 1424-8220. DOI: 10.3390/s18082468. [Online]. Available: %5Curl%7Bhttps://www.ncbi.nlm.nih.gov/pmc/articles/PMC6111879/%7D.
[9] P. K. W. Yaakov Bar-Shalom and X. Tian, *Tracking and data fusion: a handbook of algorithms, by Yaakov Bar-Shalom, Peter K. Willett and Xin Tian*. YBS Publishing, 2011, ISBN: 9780964831278.

BIOGRAPHY

Oliver Hasler *received a B.Sc. degree in mechanical engineering from ZHAW / Switzerland, a M.Sc. degree in aerospace engineering from RWTH Aachen University / Germany. He has gathered approximately seven years of industry experience in the aerospace and defense industry before becoming a PhD candidate at the NTNU University / Norway in engineering cybernetics.*

Torleiv H. Bryne *received her B.S. degree in Electrical Engineering in 1985 and a Ph.D. in Aerospace Engineering from the Massachusettes Institute of Technology in 1990. She is currently a professor of Aerospace Engineering at the University of Nowhere. Her interests include secure communications and space exploration.*

Tor Arne Johansen *ris a professor at the Department of Engineering Cybernetics. He has a MSc (1989) and a PhD (1994) in Engineering Cybernetics from NTNU. Professor Johansen is also a key scientist at the Centre for Autonomous Marine Operations and Systems (AMOS). See: http://folk.ntnu.no/torarnj/ for more information.*